Simulation of the pressure drop across granulated mixtures using a coupled DEM – CFD model

A.M. Nyembwe, R.D. Cromarty and A.M. Garbers-Craig*

Centre for Pyrometallurgy, Department of Materials Science and Metallurgical Engineering, University of Pretoria, Private Bag X20, Hatfield 0028, South Africa

*Corresponding author.

E-mail addresses:Alain.Nyembwe@tuks.co.za(A.M. Nyembwe),robert.cromarty@up.ac.za(R.D. Cromarty),andrie.garbers-craig@up.ac.za(A.M. Garbers-Craig).

Highlights

• Concentrate and micropellets decrease the permeability of a iron ore sinter bed.

• Modelled and measured pressure drops across beds of granules agreed well.

• The definition of the adhesion force is crucial when simulating the pressure drop.

• The particle shape has a strong effect on the pressure drop.

Abstract

The sinter process converts mixtures of iron ore, iron ore fines and fluxes into a fused aggregate (sinter) that is used as burden material in the blast furnace. The rate of this process is predicted by measuring the pressure drop across the green granulated mixture before ignition. A lower pressure drop corresponds with a higher permeability resulting in a higher sinter rate. The addition of fine material, such as concentrate or concentrate agglomerated into micropellets, to the sinter mixture affects the pressure drop. This study numerically predicts the pressure drop over several granulated mixtures in order to reduce the number of experimental measurements. The pressure drop was studied both experimentally using a pot grate and by coupled DEM (Discrete Element Method) – CFD (Computational Fluid Dynamics) simulations. The validation of the model was performed by comparing the measured and numerical values of the pressure drop across glass beads 3 and 6 mm in diameter respectively. The simulation of the pressure drop was extended to granulated mixtures that contain 0–40% concentrate or micropellets. DEM was also used to numerically simulate iron ore granules and relate their mechanical behaviour to particle size distribution, shape, friction coefficient, Young's modulus and adhesion force.
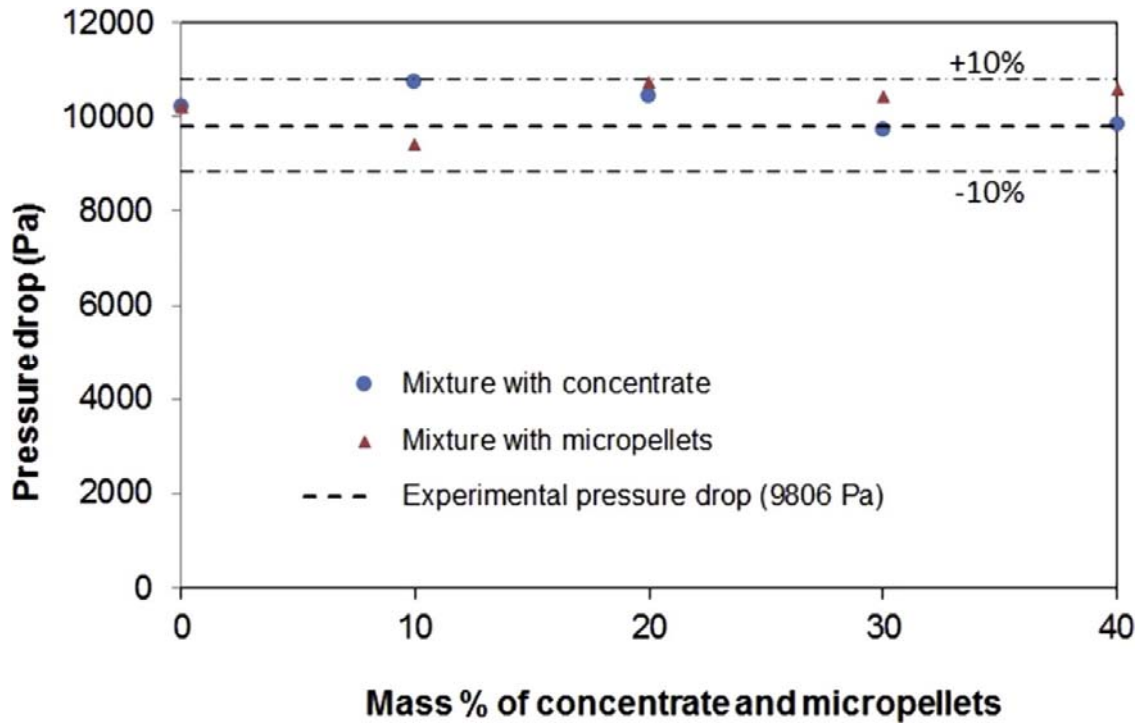
Graphical abstract

1. Introduction

During the iron ore sintering process, granules are agglomerated by heat exchange and partial fusion that are driven by suction of hot gas through the packed bed of moist granules. The pressure drop over green granules has been used to predict the rate at which the sinter process progresses and the productivity (performance) of the sinter plant. It is well known that granule beds with low pressure drop provide more stable operation and good controllability of the sintering process [1], [2], [3], [4]. In practice, the pressure drop across green granules is generally measured in Japanese Permeability Unit (JPU), and expressed by the relation [5]:

$$\text{Permeability} = \frac{F}{A}\left(\frac{L}{\Delta P}\right)^{0.6} \tag{1}$$

where F, A, L and ΔP are flow-rate of gas in m^3/min, cross sectional area of the bed in m^2, height of the bed in m and pressure drop expressed in mm H_2O.

The measurement of the pressure drop through green granules before ignition is carried out experimentally. This technique has remained an "empirical art" in most sinter plants, due to the complexity of the mixtures consisting of moist deformable granules of randomly distributed irregular shapes, structures and sizes. These parameters were known to significantly affect the void fraction, angle of repose and permeability of packed beds [3], [6], [7], [8], [9], [10], [11], [12], [13]. Zhou et al. [14] studied the pressure drop across a sinter bed during a pilot – scale – sintering process. CFD simulations were performed based

2

on the reconstructed real geometry of sinter cakes by X-ray micro-tomography. For simplicity, a sample of 30 * 30 * 30 mm^3 was excavated from the sintered zone in the centre region of the sinter cake, where the melt is supposed to solidify and no changes in structure occur. To obtain reliable values of the pressure drop (permeability), it was appropriate to simulate a large size of the sinter cake, which could unfortunately result in huge computational costs. Mitterlehner et al. [15] predicted the fluid flow through a granulated material using the Ergun equation, and adjusting the Ergun constants using the least square fit method. Very good agreement was obtained between the measured and calculated pressure drops.

Coupling of the Discrete Element Method (DEM) with Computational Fluid Dynamics (CFD) has been extensively used in the prediction of flow characteristics through packed beds [16], [17], [18]. Eppinger et al. [18] developed a numerical model of fixed bed reactors with small tube to particle diameter ratios. DEM-code was used to simulate the packing in a fixed bed consisting of randomly packed spherical particles. The fluid domain was meshed and solved with the commercial CFD-code STAR-CCM+. The predicted porosity and pressure drop was in agreement with measured data in the literature. Bai et al. [17] developed a DEM-CFD model for the simulation of the flow field and pressure drop in fixed bed reactors with randomly packed catalyst particles. The predicted pressure drop compared satisfactorily with the experimental measurements with errors of less than 10%, which is acceptable for industrial packed bed reactors [16], [17].

The prediction of the pressure drop through packed beds is significantly affected by the structure of the bed, which in turn is dependent on the particle size distribution and shape and interactions between particles [10], [19], [20], [21], [22], [23]. The difference in particle size can lead to size segregation through the percolation mechanism whereby fines can sift through the voids of larger particles [19]. A narrower particle size distribution results in looser packing than when wider size distributions are used. Particle shape also plays a major role in packing density [24], [25], [26]. Increasing angularity increases the flow resistance of particles and increases the fluid flow across the packing. Spherical shapes are simple to implement in 3D modelling and fast computationally. However, the spheres cannot reproduce the particle interactions that are observed in real-world particles. Spheres roll continuously and have lower shear resistances and lower friction coefficients than those of irregular and non-spherical particles [21], [27], [28], [29].

This paper describes a study on the applicability of using a DEM-CFD coupling model to calculate the pressure drop across a green bed of granules. The design of the packing was simulated using the discrete element method (DEM), in which the effects of the size distribution, shape and adhesion force of moist granules were considered. A multiphase flow model was used to simulate the gas flow through the simulated granule bed. Pressure drop predictions were compared against measured experimental data for granulated mixtures that contained 0–40% concentrate or micropellets respectively. Concentrate is a fine hematite-based (90.3% Fe_2O_3) iron ore, which is produced through the beneficiation of low-grade iron ore using crushing, milling and dense media separation to upgrade the ore. It has a particle size of less than 0.1 mm. The micropellets (1–4.75 mm in diameter) were produced from concentrate by rolling moist concentrate together with binders, on an

inclined disc pelletiser. With the depletion of high-grade lump iron ore, concentrate and micropellets have been identified as alternative raw materials for sintermaking.

2. DEM – CFD model

The pressure drop across complex packed beds can be simulated by using a coupled DEM-CFD model. The discrete element method is used to simulate the filling process of a column with particles [30]. The motion of a rigid particle is computed by numerically solving the Newton equations for translational and rotational motion (Eqs. (2) and (3)). Computational fluid dynamics has proven to be an alternative to empirical and experimental methods to compute the pressure drop through packed beds [31], [32], [33], [34]. For an incompressible fluid flow, CFD solves Navier-Stokes conservation equations of mass and momentum (Eqs. (4) and (5)) [35], [36]. The governing motion and conservation equations are reported in Table 1.

Table 1. Equations used in the DEM-CFD model.

Equations of translation and rotation motion

$$m_i \frac{dv_i}{dt} = F_i \tag{2}$$

$$I_i \frac{dw_i}{dt} = T_i \tag{3}$$

Conservation equations of momentum and mass

$$\left(\frac{\partial v}{\varepsilon \partial t} + \frac{1}{\varepsilon^2}(v. \nabla v) \right) = -\nabla p + \mu \nabla^2 v + \rho g + F^T \tag{4}$$

$$\frac{\partial (\rho \varepsilon)}{\partial t} + \nabla.(\rho \varepsilon v) = 0 \tag{5}$$

I_i momentum of inertia of particle i.

F_i interaction, drag and gravitational forces exerted on particle i.

F^T interphase momentum transfer term between particles and fluid.

g gravitational acceleration.

m_i mass of particle i.

p fluid pressure.

T_i torque exerted by particles on particle i.

v fluid velocity.

v_i velocity of particle i.

w_i angular velocity of particle i.

ε bed porosity.

ρ fluid density.

µ fluid viscosity.

Each particle is exposed to interactions with other particles and boundaries. These interactions are simulated using a soft particle model where the rigid particles are allowed to slightly overlap at the contact point (Fig. 1) [21]. This overlap (δ) is smaller than the particle radius and represents the elastic deformation of particles under a variety of loading conditions [21], [37], [38], [39], [40]. There are different models that account for the interactions (contact forces and adhesion forces) between each pair of particles [37], [38], [39], [40]. The simple contact force model is the linear spring – dashpot model that include springs, dashpots and frictional sliders (Fig. 2). The spring stiffness (k) and dashpot coefficient (η) are expressed through Young's modulus parameter and coefficient of restitution (ε) respectively. The frictional sliders represent the friction between contact points which is implemented with a friction factor µ [38], [41], [42].
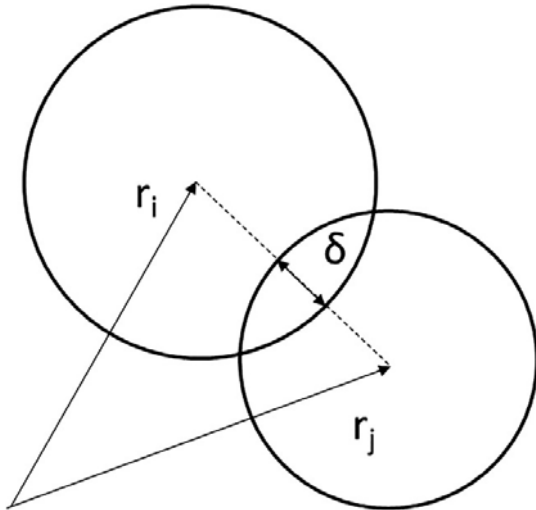

Fig. 1. Two-particle contact with overlap in normal direction. r_i and r_j are the positions of particles i and j respectively [21].
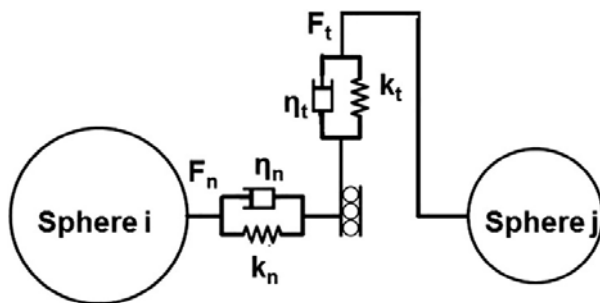

Fig. 2. Spring dashpot model for contact forces between particles [38].

There are different models that account for the interactions (contact forces and adhesion forces) between each pair of particles [37], [38], [39], [40]. The simple contact force model

is the linear spring – dashpot model (Fig. 2). The spring stiffness (k) and dashpot coefficient (η) are expressed through Young's modulus parameter and coefficient of restitution (ε) respectively. The friction sliders represent the friction between contact points which is implemented with a friction factor μ [38], [41], [42].

The normal and tangential forces can then be calculated from the relations [38]:

$$F_n = k_n \delta_n + 2\beta\sqrt{m_{ij} k_n} v_n \tag{6}$$

$$F_t = \min\{\mu F_n, k_t \int v_t dt + \sqrt{m_{ij} k_t} v_t\} \tag{7}$$

where $\beta = -\dfrac{\ln(\varepsilon)}{\sqrt{\pi^2 + \ln^2(\varepsilon)}}$ and $m_{ij} = \dfrac{m_i m_j}{m_i + m_j}$ are the dashpot ratio and reduced mass of particles i and j with masses m_i and m_j respectively. The particles are allowed to overlap and the maximum overlap δ_n between two particles is determined by the stiffness of the spring in the normal direction. The normal and tangential surface velocities are v_n and v_t respectively. The total tangential force F_t is limited by the Coulomb frictional limit μF_n.

The behaviour of wet granules is complex and the interactions between particles may be a combination of elasto-plastic deformation, viscous dissipation, and adhesion [43], [44], [45]. Previous studies used the contact bond model to simulate the adhesion between iron ore granules [22], [23], [46]. A schematic representation of the contact bond model is given in Fig. 3.
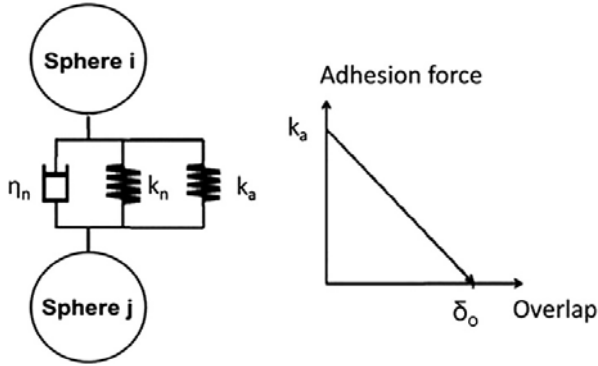

Fig. 3. Contact bond model for sticky material [22], [23], [46].

For two colliding spherical granules, the adhesion force can be expressed by Eq. (8):

$$A = k_a(\delta_0 - \delta) \tag{8}$$

where k_a is the adhesive coefficient, δ is the overlap and δ_0 is the overlap when the adhesion force (k_a) equals 0. The adhesion force reaches its maximum when the two granules touch each other. The model can return to a simple linear spring model if $k_n = k_a$ [39].

In Rocky DEM, an adhesion normal contact model is a built-in function that can capture the particle-particle interactions for wet and sticky granules. The contact forces are time-

dependent and can increase the adhesion and stiffness after initial contact. The magnitude of the normal adhesive force ($F^t_{n,adh}$) is given by [47]:

$$F^t_{n.adh} = \text{if } 0 - \Delta\delta_n \geq \delta_{adh} \tag{9}$$

$$F^t_{n.adh} = f_{adh} * \min(m_i, m_j)*g \text{ if } -\Delta\delta_n < \delta_{adh} \tag{10}$$

$$\Delta\delta_n = \delta^t_n - \delta^{t-dt}_n$$

$$\text{if } \Delta\delta_n < 0, \text{particles separate}$$

$$\Delta\delta_n > 0, \text{ particles approach each other} \tag{11}$$

Where $F^t_{n.adh}$ is the normal adhesive contact force at the current time, t; $\Delta\delta_n$ is the difference between the contact normal overlap values at the previous time (δ^{t-dt}_n) and current time (δ^t_n); f_{adh} is the adhesion force fraction and g is the gravitational acceleration. $\delta_{n,l}$ is the maximum normal overlap beyond which there is no adhesion between particles. If the force fraction is 1.0, the adhesive force will be equal to the gravity force applied to the particle. In practice, Rocky DEM uses force fractions between 0 (0%) and 0.5 (50%) in simulations to reproduce the real beha viour of wet and sticky particles. The implementation of the adhesion model in Rocky is based on the measurement of the two parameters:

- Minimum distance between particles before the adhesive forces are applied
- Adhesive force expressed in terms of fraction of the particle gravitational force.

The coupling of DEM with CFD model is achieved through the momentum transfer between particles and the fluid phase. It is therefore crucial to define the interaction forces between the two phases, which can either be from a hydrostatic source (buoyancy) or a hydrodynamic source (drag force, the virtual mass force and the lift force) [47], [48], [49], [50], [51]. In this study, the drag force F^d was considered the dominant interaction force between the solid and fluid phases. The drag force exerted by a single particle on the fluid phase is given by Eq. (12):

$$F^d = \tfrac{1}{2}\rho C_d A_p |v - u|(v - u) \tag{12}$$

where ρ is the fluid density, C_d is the drag coefficient, A_p is the projected area of the particle, v is the velocity of the fluid and u is the velocity of the particle. For densely distributed solid particles, Gidaspow et al. [49] proposed an equation through which C_d can be calculated (Eq. (13)). It represents a single drag law that is a combination of correlations developed by Wen and Yu [50] and Ergun [51]. This law can be apply over a broader range of solids volume fractions. In the DEM-CFD model the drag coefficient is available to the user as a built-in field function [47].

$$C_{\mathrm{d}} = \begin{cases} \frac{24}{\alpha_{\mathrm{f}} Re_{\mathrm{p}}} \left[1 + 0.15(\alpha_{\mathrm{f}} Re_{\mathrm{p}})^{0.687} \right] \alpha_{\mathrm{f}}^{-1.65} & \alpha_{\mathrm{f}} Re_{\mathrm{p}} < 1000; \ \alpha_{\mathrm{f}} > 0.8 \\ 0.44 \alpha_{\mathrm{f}}^{-1.65} & Re_{\mathrm{p}} \geq 1000; \ \alpha_{\mathrm{f}} > 0.8 \\ 200 \frac{\alpha_{s}}{\alpha_{\mathrm{f}} \varphi^{2} Re_{\mathrm{p}}} + \frac{7}{3\varphi} & \alpha_{\mathrm{f}} \leq 0.8 \end{cases} \tag{13}$$

where α_{f} is fluid mass percentage, α_{s} is the particles mass percentage, ϕ is the particle sphericity and Re_{p} is the Reynolds number of the particle.

3. Experiment

3.1. Glass beads

Glass beads with diameters of 3 and 6 mm (Promak Chemicals) were used in this study to validate the coupled DEM-CFD model. The diameter of 30 beads of each group was measured with a digital calliper and their average diameters were calculated. The bulk densities of the glass beads were measured by randomly filling a cylindrical flask (60 mm diameter) with a specific mass of glass beads and measuring the volume. The properties of the glass beads are listed in Table 2.

Table 2. Properties of the glass beads.

Bead size (mm)	Bulk density (kgm^{-3})	Diameter (mm)	
		Average	Standard deviation
3	1.54	3.00	0.03
6	1.51	5.94	0.09

3.2. Raw materials used

Three types of mixtures were studied: a conventional mixture (base case) and mixtures with the addition of 10–40% concentrate or micropellets respectively. Each mixture consisted of iron ore fines (<10 mm particle size), return fines, coke breeze, limestone and dolomite (Table 3). The base case mixture contained no concentrate nor micropellets, while the other mixtures also contained either concentrate or micropellets in varying amounts. The concentration of the return fines and coke breeze was kept constant, while the limestone and dolomite content was varied to achieve a CaO/SiO$_2$ mass ratio of 1.95 and MgO content of 1.81% MgO.

Table 3. Compositions of the mixtures.

Composition (mass%)

	Iron ore 1	Iron ore 2	Concentrate	Micro pellets	Return fines	Coke	Lime-stone	Dolo-mite
Base case	27.10	27.10	0.00	0.00	25.00	4.80	10.80	5.20
10%concentrate	24.53	24.53	5.47	0.00	25.00	4.80	10.43	5.23
20%concentrate	21.93	21.93	10.97	0.00	25.00	4.80	10.10	5.27
30%concentrate	19.30	19.30	16.57	0.00	25.00	4.80	9.70	5.33
40%concentrate	16.67	16.67	22.20	0.00	25.00	4.80	9.33	5.33
10%Micropellets	24.57	24.57	0.00	5.47	25.00	4.80	10.37	5.23
20%Micropellets	21.97	21.97	0.00	11.00	25.00	4.80	10.00	5.27
30%Micropellets	19.37	19.37	0.00	16.60	25.00	4.80	9.60	5.27
40%Micropellets	16.70	16.70	0.00	22.27	25.00	4.80	9.20	5.33

Concentrate was produced through the beneficiation of lower-grade iron ore resources using dense medium separation (DMS). The concentrate had a d_{50} of 0.12 mm. Micropellets were formed by pelletization of moist concentrate together with 0.5% bentonite and 0.5% polyvinyl acetate as binders, on an inclined disc. After their discharge, the micropellets were subjected to natural drying in order to minimize the costs related to heat hardening. The micropellets were spherical, with a d_{50} of 3.3 mm (Fig. 4).
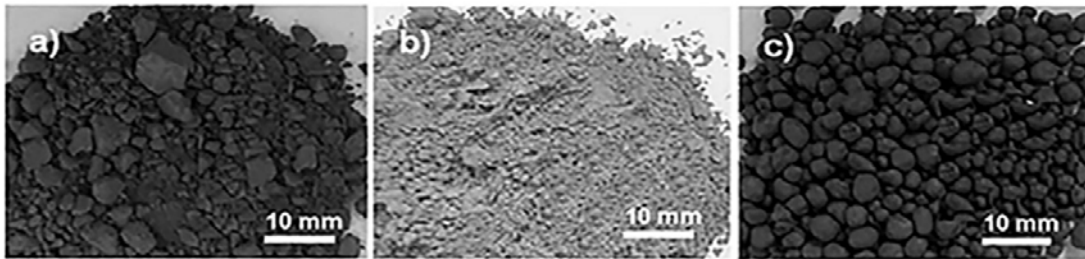

Fig. 4. Images of raw materials (a) fine iron ore (<10 mm particle size); (b) concentrate (<100 μm particle size); (c) micropellets (<5 mm particle size).

3.3. Granulated mixtures

Granules were produced by granulation of different iron ore mixtures using a bench tumbling drum of diameter 0.5 m and length 0.4 m. The velocity speed was set at 20 rpm throughout the granulation tests. The volume fill ratio was 20–21%. The sprinkling of water onto cascading particles causes the adhesion of finer particles onto coarse particles which results in the formation of large granules [20], [52], [53]. The optimum moisture content was defined as the moisture content associated with maximum permeability. An optimum

moisture content of 5.5% was associated with the base case mixture, the mixtures that contained concentrate as well as the mixture that contained 10% micropellets (Table 4). Mixtures that contained 20–40% micropellets required additional water to achieve maximum permeability, due to the inherent porosity of the pellets. Only granulated mixtures obtained at optimum moisture were considered in this study.

Table 4. Granule size distributions and Sauter mean diameters of mixtures obtained at optimum moisture.

Mixtures	Optimum moisture	Granule size distribution (mass% retained)						Sauter mean diameter (mm)
	(%)	+4.75 mm	+2.00 mm	+1.00 mm	+0.50 mm	+0.25 mm	Pan	
Base case mixture[*]	5.5	51.00	39.64	7.85	1.23	0.18	0.08	3.78
10% concentrate	5.5	45.48	41.80	10.68	1.71	0.23	0.10	3.44
20% concentrate	5.5	31.26	53.76	12.85	1.87	0.21	0.04	2.75
30% concentrate	5.5	32.54	47.20	15.59	3.98	0.56	0.14	2.66
40% concentrate	5.5	17.42	58.30	19.02	4.10	0.88	0.27	2.48
10% micropellets	5.5	32.52	46.26	16.05	4.35	0.56	0.27	2.61
20% micropellets	6.0	15.35	58.75	20.87	4.08	0.64	0.31	2.41
30% micropellets	6.0	24.40	51.56	18.57	4.47	0.72	0.29	2.51
40% micropellets	6.5	30.14	55.63	12.10	1.84	0.25	0.04	3.13

*Base case mixture: Mixture without addition of concentrate or micropellets.

Granulated mixtures were categorized in different size fractions using five sieves with aperture diameters of 4.75 mm, 2 mm, 1 mm, 0.5 mm, 0.25 mm respectively (Table 4). For each sample, the Sauter mean diameter was calculated from the granule size distribution (GSD) of the granulated mixture by the relation:

$$d_p = \frac{100}{\sum_i \frac{x_i}{d_{pi}}} \tag{14}$$

where d_{pi} is the mean granule diameter for size fraction i and x_i is the mass percentage (wet basis) of granules of size fraction i.

Granule samples were subjected to X-ray micro-tomographic analysis to reveal their 2D internal structures and mechanisms of granulation. Four groups of structures were then identified (Fig. 5). Granules of Group I (Gr I) was obtained by the common process where the finer fraction (<0.25 mm) of the feed material adhered onto coarse particles (Fig. 9a). This structure was found across all three types of granulated mixtures. The addition of concentrate resulted in the production of granules with a pellet-like structure (Gr II), which formed in a coalescence process (Fig. 5b) [54]. Granules of Group III (Gr III) formed through adhesion of micropellets and those of Group IV (Gr IV) by layering of small granules on large granules (Fig. 5c). All four structures had a sticky outer layer and exhibited surface irregularity.

Fig. 5. X-ray micro-tomographs of granules (a) base case; (b) with concentrate addition; and (c) with micropellet addition.

3.4. Pressure drop measurements

The measurement of the pressure drop was carried out using a pot grate (Fig. 6). For each test, iron ore granules were randomly poured into the pot grate (tube) to create a bed, 535 mm in height that was supported by a grid with a 1 mm diameter aperture. A venturi system was securely sealed to the top of the pot. The bottom of the pot grate was connected to a centrifugal fan using a flexible rubber tube to avoid vibrations. A manual valve was used to control the pressure drop through the packed bed. Air was then drawn through the packed bed. Pressure drop was measured in the venturi and across the packed bed, using water manometers. Airflow was adjusted to give a pressure drop across the packed bed of 1000 mm H_2O. The pressure drop in the venturi was then used to calculate the flow rate. The pressure drop across the pot grate was reported in Japanese Permeability Unit (JPU).
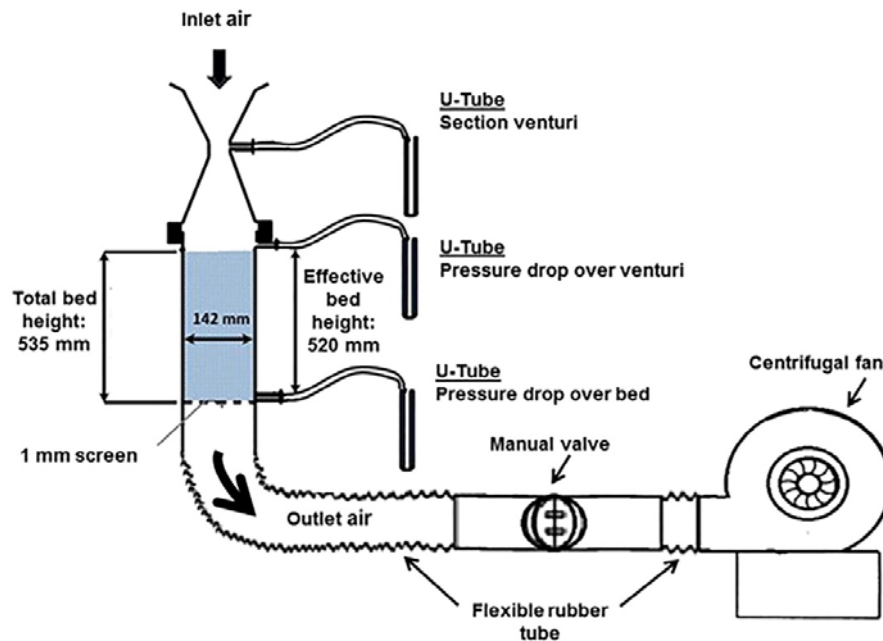
Fig. 6. Schematic representation of the pot grate.

4. Simulation procedure

4.1. Dynamic properties of glass beads and granulated mixtures

The application of the DEM – CFD model requires the measurement of the dynamic properties of particles (Static friction coefficient, restitution coefficient, Young's modulus and adhesion force). While there are numerous theoretical and numerical studies on mechanical behaviour of glass beads, only few studies on the behaviour of iron ore granules (agglomerates) are reported in the open literature [22], [23]. These granules are wet, sticky, deformable and heterogeneous, and can easily disintegrate. It is therefore a significant challenge to measure the dynamic properties of these granules.

The angle of repose (static friction coefficient) of glass beads and granules was experimentally measured using a slump test [52]. Solid particles were loosely poured into a tube and lifted to allow the granular material to a pile under gravitational forces. The angle of repose was described as the angle that the accumulated material forms with the horizontal surface (Fig. 7). The tangent of the angle of repose has been found to be equal to the internal (static) friction of the granular material. The experimental static friction coefficients are listed in Table 5. The static friction coefficient of glass beads is smaller than that of iron ore granules. Glass beads are smooth and spherical and can flow more easily than iron ore granules that are irregular and sticky.
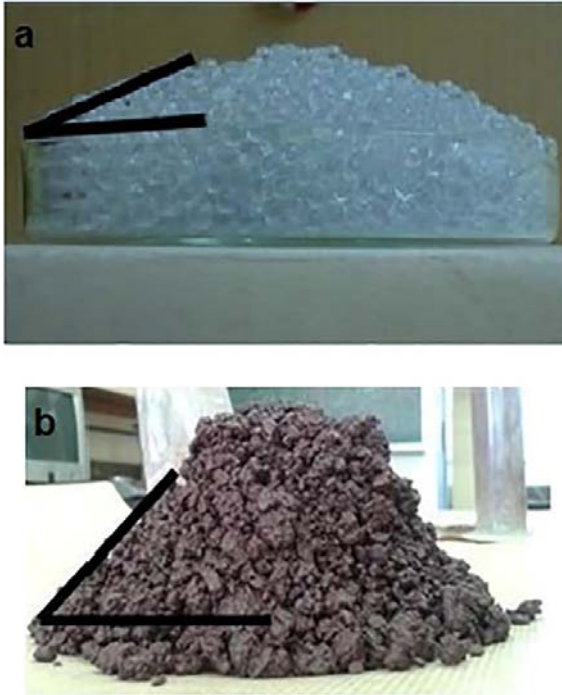
12

Fig. 7. Angle of repose for (a) 6 mm glass beads and (b) granulated mixtures where granules are sticky.

Table 5. Measured static friction coefficient of glass beads and granulated mixtures at optimum moisture content.

Mixtures	Angle of repose (°)	Static friction coefficient
Glass beads		
3 mm glass beads	21.40	0.39
6 mm glass beads	16.00	0.29
Granulated mixtures		
Base case mixture	45	1.00
10% concentrate	40	0.84
20% concentrate	42	0.90
30% concentrate	40	0.84
40% concentrate	38	0.78
10% micropellets	39	0.81
20% micropellets	40	0.84
30% micropellets	39	0.81
40% micropellets	32	0.62

The flow characteristics of the glass beads are affected by the coefficient of restitution (ε_r), which is generally a measure of energy loss during a collision. This coefficient varies between 0 and 1. The two end conditions correspond to perfectly plastic ($\varepsilon_r = 0$) and perfectly elastic impact ($\varepsilon_r = 1$) respectively. The restitution coefficient can be expressed as the square root of the ratio of elastic energy $E_{kin,reb}$ released during the rebound of the particle to the initial kinetic impact energy $E_{kin,imp}$ (Eq. (15)) [55], [56]. The restitution coefficient is measurement in a drop test. A particle is held at a determined height (h) above a flat surface and released with zero initial velocity and rotation. After its impact with the surface, the particle reaches a rebound height (h_{reb}).

$$\text{COR} = \sqrt{\frac{E_{kin, \, reb}}{E_{kin, \, imp}}} \approx \sqrt{\frac{2gh_{reb}}{2gh}} = \sqrt{\frac{h_{reb}}{h}} \tag{15}$$

The restitution drop test for each glass bead size was repeated 10 times and average values were used in DEM simulation (Table 6). The height of the drop test was set at 82 mm. The impact surface was a flat steel block with a thickness of 30 mm. The measured coefficient of restitution decreased with the size of the glass beads. For granulated mixtures, the restitution coefficient was almost zero due to the stickiness of the granules.

Table 6. Restitution coefficient of glass beads of different glass bead sizes.

Glass bead size (mm)	Mean restitution coefficient	Standard deviation
3	0.77	0.02
6	0.73	0.01

4.2. Implementation of the DEM-CFD model

A two-way coupling of DEM (Rocky 3.9) and CFD (Fluent 16.1) was used to numerically calculate the pressure drop through a 3D-modelled bed of granules. DEM is fully integrated with Ansys Fluent CFD and both solvers can run in parallel [30]. The coupled DEM – CFD model was first validated using glass beads, 3 mm and 6 mm in diameter. The simulation of the packing was performed in such a manner that the number of generated particles forms the approximate same bed height regardless of the glass bead size. Corresponding tube:particle diameter ratios (D/d_p) for 3 and 6 mm glass beads were respectively 47 and 24, which are significantly more than 10, and hence the wall effects could be neglected [16], [17]. An unstructured mesh composed of tetrahedral elements was first created in Fluent CFD and imported in Rocky DEM. The packed bed was then simulated by dropping a stream of particles into a column from a specified height. The filling process with glass beads of 3 mm in diameter is shown in Fig. 8.
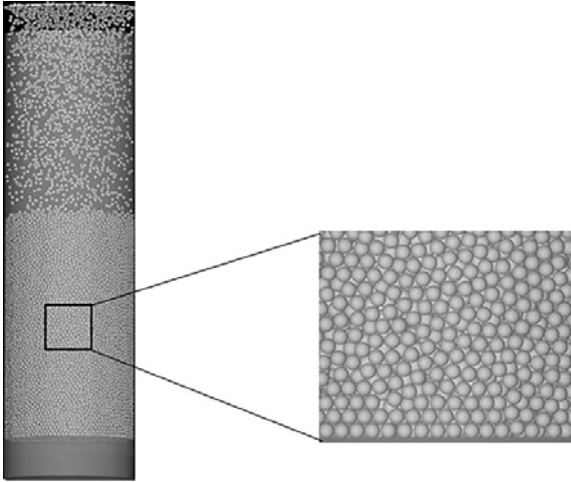
Fig. 8. DEM simulation of 3 mm glass beads.

The granules from the base case mixture were selected for validation of granule properties (size distribution, coefficient of restitution, shape, Young's modulus and adhesion force). The measurement of the stiffness (Young's modulus), coefficient of restitution and adhesion force is not evident for irregular, deformable and sticky particles. Two methods are generally used to measure the input parameters (granule properties): bulk calibration and direct measuring approaches [57], [58]. The bulk calibration approach is based on comparing the values of a specific material bulk property (for instance pressure drop) that can be obtained using an experimental setup and its numerical replica. The DEM parameter values are then adjusted until the predicted bulk response matches the measured result. The second approach consists of directly measuring the property value on particle or contact scale. This method appears to be more relevant as long as the particle property can be experimentally measured. In this paper, both methods were used to determine the values of the properties of the granules.

A simple approach was adopted herein, whereby each parameter could be changed while the other ones could be kept constant during DEM-CFD simulations [22], [23], [59]. The Young's modulus data were selected based on previous investigations of the behaviour of iron ore granules and pellets. The simulation of the collapse of the granule bed on the sintering machine was effectively achieved by choosing a range of Young's modulus between 1 and 10 MPa [22], [23]. Wang et al. [59] investigated the bulk behaviour of green iron ore pellets in an industrial pelletizing system, using the non-smooth discrete element method (NDEM). Experimental and simulation results were comparable for a Young's modulus of 6.2 MPa.

The adhesion force was expressed in terms of a force fraction, which could vary from 0 to 0.5 [47]. The measured coefficients of restitution were closer to zero due the stickiness and ease of disintegration of green granules. The coefficient of restitution was therefore set to the lowest default value (0.1) that Rocky can capture [30]. Spheres, rounded polygons and polyhedrons were used to represent the irregularity of the granules. The custom shapes with overlapping spheres were not considered due to the limit of available computational resources. The rolling resistance was implemented in DEM to account for the particle shape

effect on the overall behaviour of the granular flow. The size distribution and friction coefficient of granules were captured as raw data obtained from sieving of partially dried granules and slump tests, respectively. The input parameters for DEM-CFD simulation of the pressure drop through the base mixture are specified in Table 7. The DEM packing was scaled down by setting the column-to-glass bead diameter ratio (D/d_p) and glass bead diameter-to-packing height ratio (d_p/H) to be larger than 10 and less than 0.05 respectively [56]. The packing was then reduced to column packing with a diameter of 70 mm and height of 200 mm.

Table 7. DEM-CFD parameters for glass beads and base case mixture.

Parameters (units)	Value		
	Glass beads		Base case mixture
	3 mm	6 mm	
Granule density (kg/m^3)	1520		2000
Granule shape	Sphere		Sphere, rounded polygon and polyhedron
Force fraction (–)	0		0.05; 0.1: 0.2; 0.3; 0.5
Young's modulus (GPa)	10^7		0.1–1
Rolling resistance (default)	0		0.15
Coefficient of restitution (–)	0.77	0.73	0.1
Static friction coefficient (–)	0.39	0.29	1.0
Air velocity (m/s)	2.01	1.41	0.68
Time step (DEM; CFD) (s)	10^{-7}; 10^{-3}		6.10^{-6}; 10^{-3}

5. Results and discussion

5.1. Effect of concentrate and micropellet addition on bed permeability

The addition of concentrate or micropellets to the conventional mixture caused a decrease in the bed permeability as the volume fraction of concentrate or micropellets increased (Fig. 9). The presence of concentrate or micropellets resulted in the formation of additional granule structures: Concentrate addition produced granules of Groups I and II, which can potentially deform once packed in a column [52], [54]. This resulted in formation of compact beds with low permeability. The addition of micropellets led to the formation of small granules (Groups I and III) as well as weak big granules (Gr IV) (Fig. 5). The presence of these granules was the cause of the decrease in the bed permeability [3], [8], [52].
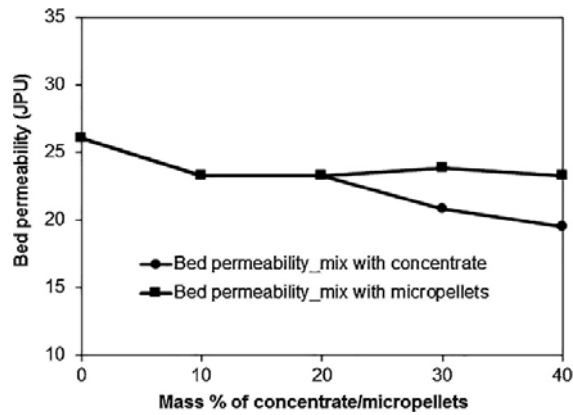
Fig. 9. Variation of the maximum permeability with concentrate or micropellet addition at optimum moisture content.

5.2. Mesh size dependency

The specification of mesh size is an important part in CFD, especially in complex geometries such as those found in packed beds [36], [60]. Although the mesh size must be fine to describe enough detail of the flow through the bed, it must also be coarse enough to complete the simulation in reasonable time. To study the effect of mesh size on the pressure drop over a packed bed of glass beads, several numerical simulations with different mesh sizes were conducted while the particle size was held constant for each type of glass bead. A series of mesh sizes (6 mm, 12 mm, 24 mm, 36 mm and 48 mm) were selected in such a way that several particles could fit inside one CFD mesh element [36], [60]. The results showed that the pressure drop through the packed beds decreased with increasing mesh size (Fig. 10). It can also be seen that the pressure drop is almost independent of mesh size when it is larger than 24 mm.
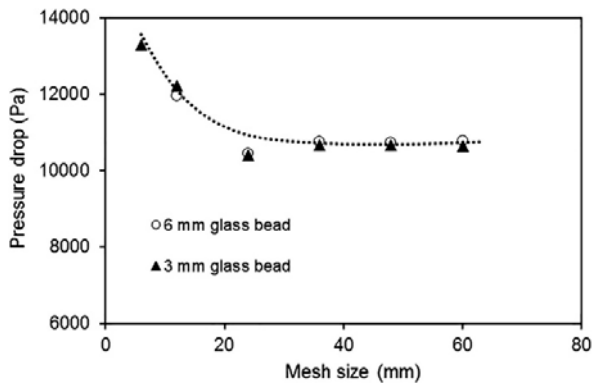

Fig. 10. Effect of mesh size on pressure drop across beds of glass beads.

The deviations between the simulated and measured pressure drops were also plotted against the mesh size (Fig. 11). It can be seen that the deviation is virtually constant for a mesh size of 36 mm and larger, and within ±10%. An unstructured mesh (tetrahedral) of 36 and/or 48 mm mesh size was therefore chosen for further simulations of the pressure drop.
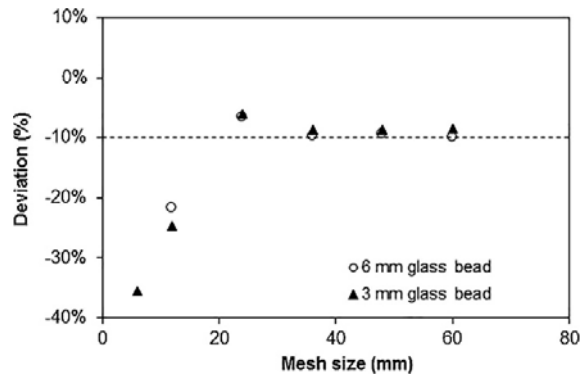
17

Fig. 11. Deviation between the simulated and measured pressure drops with mesh size.

5.3. Validation of the model using glass beads

The validation of the DEM-CFD model was carried out by comparing the model output with measured pressure drops over packed beds of glass beads (Table 8). The accuracy was within 10%, which shows that the model can be applied to the simulation of pressure drops over glass beads loaded into a pot grate. Good agreement was also obtained for binary mixtures constituted of 3 mm and 6 mm glass beads. The simulations overpredicted the pressure drops across all the examined mono-sized beds. Since the top surface of the DEM packed bed was not well levelled, the packed bed was extended of 0.2–3% above the target height in order to measure the pressure drop at a height of 535 mm (target value). This was the cause of the over-prediction of the pressure drop using the DEM-CFD model.

Table 8. Comparison of measured and simulated pressure drops across beds of glass beads.

Packed bed	Air velocity (m/s)	Measured pressure drop (Pa/m)	Model output (Pa/m)	Deviations (%)
Monosize mixture				
3 mm glass bead	2.01	9806	10,657	−8.68
6 mm glass bead	1.41	9806	10,760	−9.73
Binary mixture				
75% 3 mm, 25% 6 mm glass bead	1.30	9806	10,658	−8.70
50% 3 mm, 50% 6 mm glass bead	1.34	9806	10,461	−6.68
25% 3 mm, 75% 6 mm glass bead	1.44	9806	10,725	−9.38

18

5.4. Validation of the input parameters in the DEM model

Accurate predictions with the DEM model can only be achieved if the input parameter values (Young's modulus, adhesion fraction, size distribution and shape of particles) are meticulously determined. A simple approach was adopted herein, whereby each parameter was changed while the other ones were kept constant during DEM-CFD simulations [22], [23], [59]. The appropriate combinations of particle size distribution, particle shape and contact forces could therefore be chosen. The validation of Young's modulus, adhesion force, particle size distribution and shape was carried out using the physical and dynamic properties listed in Table 7.

5.4.1. Young's modulus (spring stiffness)

Young's modulus of a material describes its elastic and plastic behaviour when a force is applied. For deformable and sticky granules, Young's modulus is lower than that of dry and rigid granules [39], [58]. In this paper, the Young's modulus of iron ore granules were estimated by comparing the experimental pressure drops and measured data. Six values of Young's modulus (10^5, 1.05×10^5, 1.1×10^5, 2×10^5, 5×10^5, 10×10^5 Pa) were then assigned to the examined mixtures and simulations were run to calibrate the Young's modulus value. The size distribution of granules was truncated at 0.5 mm to reduce the number of DEM particles. An increase in Young's modulus from 10^5 to 10^6 Pa resulted in a decrease in the pressure drop through the packed bed of iron ore granules (Table 9).

Table 9. Comparison of the predicted pressure drop and measured pressure drop for different Young's moduli.

Young's modulus (Pa)	Number of granules	Air velocity (m/s)	Predicted pressure drop (Pa)	Measured pressure drop (Pa)	Deviation (%)
100,000	65,537	0.68	11,770	9806	−20.03
105,000	63,232	0.68	10,431	9806	−6.38
110,000	61,681	0.68	9500	9806	3.15
200,000	57,124	0.68	5503	9806	43.88
500,000	54,001	0.68	3776	9806	61.49
1,000,000	50,860	0.68	2563	9806	73.86

Good agreement between the measured and predicted pressure drop was achieved at Young's moduli of 105,000 and 110,000 Pa, with deviations of less than 10%. For a Young's modulus value bigger than 110,000 Pa, the deviations significantly increased. Higher stiffness values caused lower overlaps, resulting in a lower number of granules that could occupy the same volume of the column [27], [58]. Consequently, granules with a higher stiffness produced a bed with a lower pressure drop as long as the other DEM parameters (size distribution, shape, friction and restitution coefficients of granules) stayed constant. Under the current simulation conditions, an increase in Young's modulus resulted in a decrease in the number of granules in the column (Table 9).

5.4.2. Adhesion force (force fraction)

Five force fractions (0.02, 0.05, 0.1, 0.2 and 0.5) were used to study the effect of adhesion on the pressure drop over iron ore granules. The simulations were performed using spheres with equivalent size distribution of granules from the base case mixture. The spring stiffness was set to 105,000 Pa to reduce the simulation time. The simulations with different force fractions reproduced the measured pressure drop well, with deviations within 10%. For granules with no adhesion force (0% force fraction), the granules were considered as elastic particles, resulting in higher deviation (29.46%) from the measured pressure drops (Table 10). The adhesion between particles affected the pressure drop. The packed beds with adhesion were denser than the packed bed without adhesion and had high pressure drop under same simulation conditions. No significant change in pressure drop was observed when the adhesion force increased from 0.02 to 0.05.

Table 10. Comparison of the predicted pressure drop and measured pressure drop for different adhesion force fractions.

Adhesion force fraction	Air velocity (m/s)	Predicted pressure drop (Pa)	Measured pressure drop (Pa)	Deviation (%)
0	0.68	6917	9806	29.46%
0.02	0.68	10,425	9806	−6.31%
0.05	0.68	10,334	9806	−5.38%
0.1	0.68	10,431	9806	−6.37%
0.2	0.68	10,303	9806	−5.06%
0.5	0.68	10,196	9806	−3.97%

5.4.3. Fine size fraction of granules

The particle size distribution has a great influence on the computing time in DEM simulations. A simulation with particles of a narrow particle size distribution is known to run faster than broader size distributions [61]. The presence of a higher mass fraction of fine particles can increase the overall number of particles and computational costs for the same simulation conditions.

The effect of a narrower size distribution was studied by comparing pressure drops through granules with full and truncated size distributions. The cut-sieve was estimated at 0.5 mm size fraction, which commonly represents the cut-off size between adhesive fines and coarse particles. In this study, the finer size fraction (<0.5 mm) was assumed to have been broken off from the big granules during screening. Hence, two size ranges from 0 to 10 mm and 0.5 to 10 mm were considered (Table 11).

Table 11. Mass fraction of full and truncate size distributions for base mixture.

Size fraction	Mass fraction (%)	
	Full PSD	Truncated PSD
4.75–10.00 mm	51.00	51.14
2.00–4.75 mm	39.64	39.75
1.00–2.00 mm	7.86	7.88
0.50–1.00 mm	1.23	1.23
0.25–0.50 mm	0.19	0
<0.25 mm	0.08	0

The number of particles (168,500 particles) in the simulation with wider size distribution (0–10 mm size fraction) was higher than that of the equivalent system (58,089 particles) with a truncated size distribution (0.5–10 mm). The DEM simulation with wider PSD took 24.5 h to complete. The computing time was substantially shorter (~2 h) for a size distribution without the finer fraction. The presence of the finer fraction in the granule bed resulted in an increase in pressure drop, with a deviation of 17.08% between the full and truncated size distributions (Table 12). The predicted pressure drop through granules with a 0.50–10 mm size fraction was comparable to the measured pressure drop with a deviation of 6.37%, which is less than the accepted limit of 10% (Table 11).
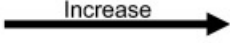
Table 12. Comparison between simulations with full and truncated size distribution.

Size distribution range (mm)	Number of particles	Air velocity (m/s)	Computing time (hours)	Predicted pressure drop (Pa)	Measured pressure drop (Pa)	Deviation (%)
0–10 mm	168,500	0.68	24.5	11,481	9806	−17.08
0.5–10 mm	58,089	0.68	2.10	10,430	9806	−6.38

5.4.4. Granule shape

It is well established that the particle shape is important to represent the behaviour of real particles in a DEM simulation. The shapes of iron ore granules are complex and difficult to be represented from a geometric point of view. Furthermore, the iron ore granules have a range of shapes. It is however not practical to implement many individual shapes in DEM. In this study, the effect of the granule shape was studied by carrying out simulations with spheres, rounded polygons (4 and 25 corners) and polyhedrons (4 and 25 corners). The examined shapes are shown in Table 13. The rounded polyhedrons are more angular than those of rounded polygons. The angularity in each shape group increases with a decrease in the number of corners.

Table 13. Examined shapes of DEM particles.

	Sphere	Rounded polygons		Rounded polyhedrons	
Shape					
Number of corners	∞	25	4	25	4
Order of angularity		Increase →			

The irregular shape of the particles prevented the formation of a dense packing. The pressure drop through packed beds decreased with a decrease in sphericity of the particles and an increase in angularity (Fig. 12). Spheres have no rolling resistance and percolate easily to form dense packed beds with higher pressure drops. The decrease in pressure drop was more significant in the case of rounded polyhedrons than that of rounded polygonal shapes. The interlocking forces are more significant in packed bed of particles with sharper corners (higher angularity) than that with rounded ones [7], [8]. Consequently rounded polyhedrons with 4 corners formed the loosest packed bed with the lowest pressure drop (Fig. 12). The predicted and measured pressure drops through spheres and rounded polygons were comparable with deviations smaller than 10%.
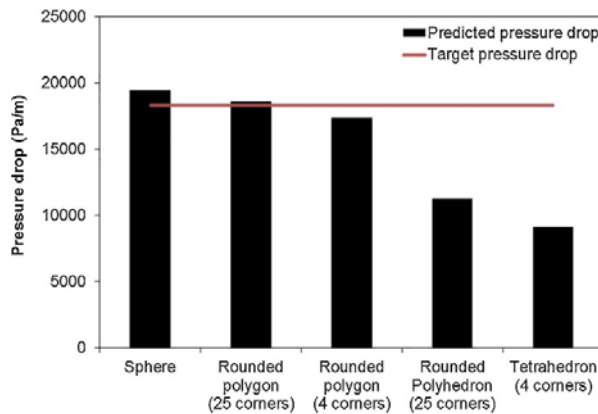

Fig. 12. Variation of pressure drop with particle shape.

5.5. DEM – CFD simulations for granulated mixtures with concentrate or micropellets

In this section, spheres with equivalent dynamic properties (stiffness, friction and adhesion) were used during DEM – CFD simulations of the pressure drop through granulated mixtures with concentrate or micropellets. The simplification of the particle shape was adopted to avoid running DEM simulations beyond available computational resources. The adhesion force was kept constant (10% force fraction). The size distribution of granules was truncated at the 0.5 mm size fraction. The truncated size distribution of the granules is given in Fig. 13. The mass fraction of +4.75 mm granule size (big granules) decreased with addition of concentrate or micropellets, while that of small size fractions (less than +4.75 mm)

increased. Addition of 40% micropellets increased the +4.75 mm size fraction due to the formation of big granules which were formed through adherence of the micropellets around large granules.
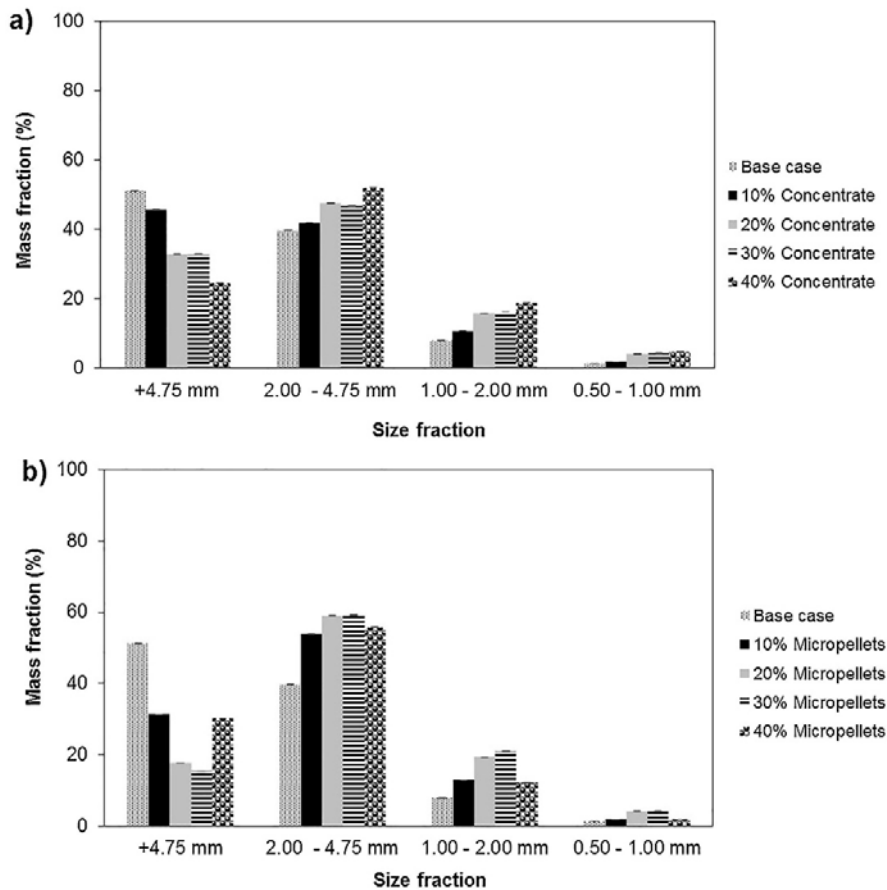

Fig. 13. Variation of size fraction with the addition of concentrate (a) or micropellets (b) at optimum moisture content.

The presence of small size fractions in multi-sized systems was reported to slightly increase the overall stiffness of the packing [62]. Guan et al. [63] found that the macroscopic Young's modulus is inversely proportional to the particle diameter for a packing of rock layers. Keppler et al. [64] reported that a decrease in the bulk friction and cohesion between particles increases the contact stiffness as well as Young's modulus. In this section, the stiffness (Young's modulus) was therefore adjusted to 130,000 Pa to account for an increase in small size fractions with addition of concentrate or micropellets as well as a decrease in bulk friction coefficient [62], [63], [64]. The density of granules varied between 2000 to 2150 kg/m^3. The addition of concentrate or micropellets (0–40%) decreased the static friction coefficient from 1 to 0.78 (45 to 38°) and 1 to 0.62 (45 to 32°) respectively for granules obtained at optimum moisture (Table 5). The flow rate of air was experimentally adjusted to obtain a constant pressure drop of 9806 Pa through all the granulated mixtures. An increase in concentrate or micropellets resulted in a decrease in the bed permeability and velocity of air through the granules (Table 14). The main input parameters that varied with addition of concentrate or micropellets are given in Table 14.

Table 14. Parameters of DEM – CFD simulations for granulated mixtures at optimum moisture content.

Mixtures	Density (kg/m³)	Stiffness (Pa)	Friction coefficient	Air velocity (m/s)
Base mixture	2000	105,000	1.00	0.68
10% Concentrate	2050	105,000	0.84	0.61
20% Concentrate	2100	130,000	0.90	0.61
30% Concentrate	2100	130,000	0.84	0.55
40% concentrate	2150	130,000	0.78	0.51
10% Micropellets	2100	130,000	0.81	0.61
20% Micropellets	2150	130,000	0.84	0.55
30% Micropellets	2150	130,000	0.81	0.55
40% Micropellets	2100	130,000	0.62	0.58

The pressure drop through different granulated mixtures was calculated by coupled DEM – CFD simulations. The number of DEM particles to fill the same packing volume increased with the addition of concentrate or micropellets (Fig. 14). This was due to an increase in small size fractions (-4.75 mm). For the granulated mixture with 40% micropellets, the number of DEM particles decreased due to a slight increase in the mass fraction of the +4.75 mm granule size.
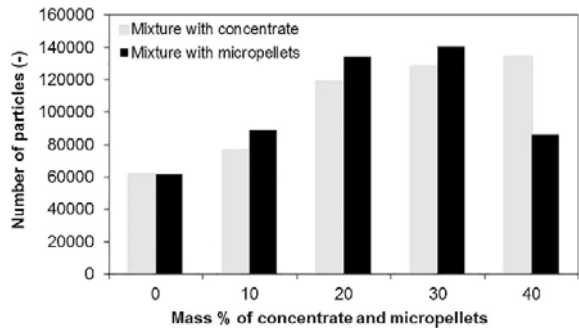

Fig. 14. Variation of the number of DEM particles with the addition of concentrate or micropellets at optimum moisture content.

The predicted and measured pressure drops were similar for stiffnesses ranging from 105,000 Pa to 130,000 Pa. The developed coupled DEM-CFD model therefore predicts the pressure drop across beds of iron ore granules well. The deviations between measured and predicted pressure drops through granulated mixtures with concentrate or micropellet addition were found to be within an acceptable accuracy of ±10% (Fig. 15).
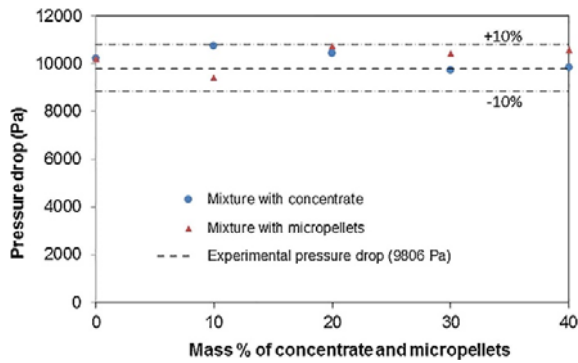
Fig. 15. Comparison between the measured and predicted pressure drops through granulated mixtures with addition of concentrate or micropellets at optimum moisture content.

6. Conclusions

Experimental measurements and coupled DEM – CFD simulations of pressure drops across beds of iron ore granules were investigated in this study. Based on the experimental results, four structures of iron ore granules were identified. Granules of Group I were formed through adhering of fines around coarse particles. With addition of concentrate, the coalescence of fine material formed granules with pellet-like structure (Group II). The addition of micropellets resulted in the formation of two additional structures. The micropellet-micropellet and micropellet-large granule adhesion produced granules of Group III and Group IV respectively. The different structures were considered the cause of the increase in pressure drop resulting in a decrease in the bed permeability.

Validation of the DEM-CFD model was realized by comparing the measured pressure drops across glass beads with the simulated data. The application of the model was extended to granulated mixtures with addition of concentrate or micropellets. The effects of Young's modulus, adhesion fraction, particle size distribution and shape on the pressure drop were well recognized. The definition of the adhesion force and shape was crucial in the simulation of pressure drop across iron ore granules. Additionaly, good agreement was achieved between the model output and measured pressure drops across beds of granulated mixtures that contain concentrate or micropellets for Young's moduli between 0.105 and 0.110 MPa.

Acknowledgements

References

[1] B.G. Ellis, C.E. Loo, D. Witchard. Effect of ore properties on sinter bed permeability and strength. Ironmak. Steelmak., 34 (2007), pp. 99-108, 10.1179/174328107X165726

[2] J. Khosa, J. Manuel. Predicting granulating behaviour of iron ores based on size distribution and composition. ISIJ Int., 47 (2007), pp. 965-972, 10.2355/isijinternational.47.965

[3] W.J. Rankin, P.W. Roller, R.J. Batterham. Quasi-particle formation and the granulation of iron ore sinter feeds. Proc. Jt. Symp.ISIJ AIMM, Tokyo, Japan (1983), pp. 13-28

[4] D.F. Ball, J. Dartnell, J. Davison, A. Grieve, R. Wild. Agglomeration of Iron Ores. Heinemann Educational Books Ltd, London (1973)

[5] E.W. Voice, S.H. Brooks, P.K. Gledhill. The permeability of sinter beds. J. Iron Steel Inst., 174 (1953), pp. 136-139

[6] J.T. Carstensen, P.-C. Chan. Relation between particle size and repose angles of powders. Powder Technol., 15 (1976), pp. 129-131, 10.1016/0032-5910(76)80037-X

[7] J. Hinkley, A.G. Waters, J.D. Litster. An investigation of pre-ignition air flow in ferrous sintering. Int. J. Miner. Process., 42 (1994), pp. 37-52, 10.1016/0301-7516(94)90019-1

[8] J. Hinkley, A.G. Waters, D. O'Dea, J.D. Litster. Voidage of ferrous sinter beds: new measurement technique and dependence on feed characteristics. Int. J. Miner. Process., 41 (1994), pp. 53-69, 10.1016/0301-7516(94)90005-1

[9] R. Soda, A. Sato, J. Kano, E. Kasai, F. Saito, M. Hara. Analysis of granules behavior in continuous drum mixer by DEM. ISIJ Int., 49 (2009), pp. 645-649

[10] E. Kasai, W.J. Rankin, J.F. Gannon. The effect of raw mixture properties on bed permeability during sintering. ISIJ Int., 29 (1989), pp. 33-42, 10.2355/isijinternational.29.33

[11] A. Van Burkalow. Angle of repose and angle of sliding friction: An experimental study. Bull. Geol. Soc. Am., 56 (1945), pp. 669-707, 10.1130/0016-7606(1945) 56[669:AORAAO]2.0.CO;2

[12] J. Wooten. Dense and sock catalyst loading compared. Oil Gas J., 12 (1998), pp. 66-70

[13] Y.C. Zhou, B.D. Wright, R.Y. Yang, B.H. Xu, A.B. Yu. Rolling friction in the dynamic simulation of sandpile formation. Phys. A Stat. Mech. Appl., 269 (1999), pp. 536-553, 10.1016/S0378-4371(99)00183-1

[14] H. Zhou, M. Zhou, M. Cheng, W. Guo, K. Cen. Experimental study and X-ray microtomography based CFD simulation for the characterization of pressure drop in sinter bed. Appl. Therm. Eng., 112 (2017), pp. 811-819

[15] J. Mitterlehner, G. Loeffler, F. Winter, H. Hofbauer, H. Schmid, E. Zwittag, T.H. Buergler, O. Pammer, H. Stiasny. Modelling and simulation of heat front propagation in the iron ore sintering process. ISIJ Int., 44 (2004), pp. 11-20

[16] H. Bai, J. Theuerkauf, P. Witt, P. Gillis. Modelling fluid flow and pressure drop in packed beds with coupling DEM and CFD. AIChE 2004 Fall Annu. Meet., Nov 7–9, 2004, Austin, Texas (2004)

[17] H. Bai, J. Theuerkauf, P.A. Gillis, P.M. Witt. A coupled DEM and CFD simulation of flow field and pressure drop in fixed bed reactor with randomly packed catalyst particles. Ind. Eng. Chem. Res., 48 (2009), pp. 4060-4074, 10.1021/ie801548h

[18] T. Eppinger, K. Seidler, M. Kraume. DEM-CFD simulations of fixed bed reactors with small tube to particle diameter ratios. Chem. Eng. J., 166 (2011), pp. 324-331, 10.1016/j.cej.2010.10.053

[19] A.B. Yu, N. Standish. Porosity calculations of multi-component. Powder Technol., 2 (1987), pp. 233-241

[20] W.J. Rankin, P.W. Roller, R.J. Batterham. Analysis of the permeability of granulated iron sinter feeds using the ergun equation. Miner. Metall. Process., 53–59 (1985)

[21] P.A. Cundall, O.D.L. Strack. A discrete numerical model for granular assemblies. Géotechnique, 29 (1979), pp. 47-65, 10.1680/geot.1979.29.1.47

[22] M. Nakano, T. Abe, J. Kano, K. Kunitomo. DEM analysis on size segregation in feed bed of sintering machine. ISIJ Int., 52 (2012), pp. 1559-1564, 10.2355/isijinternational.52.1559

[23] S. Ishihara, R. Soda, Q. Zhang, J. Kano. DEM simulation of collapse phenomena of packed bed of raw materials for iron ore sinter during charging. ISIJ Int., 53 (2013), pp. 1555-1560, 10.2355/isijinternational.53.1555

[24] K. Vollmari, T. Oschmann, S. Wirtz, H. Kruggel-Emden. Pressure drop investigations in packings of arbitrary shaped particles. Powder Technol., 271 (2015), pp. 109-124, 10.1016/j.powtec.2014.11.001

[25] R. Caulkin, W. Tian, M. Pasha, A. Hassanpour, X. Jia. Impact of shape representation schemes used in discrete element modelling of particle packing. Comput. Chem. Eng., 76 (2015), pp. 160-169, 10.1016/j.compchemeng.2015.02.015

[26] P.W. Cleary. Industrial particle flow modelling using discrete element method. Eng. Comput., 26 (2009), pp. 698-743, 10.1108/02644400910975487

[27] C.J. Coetzee. Calibration of the discrete element method and the effect of particle shape. Powder Technol., 297 (2016), pp. 50-70, 10.1016/j.powtec.2016.04.003

[28] X. Lin, T.T. Ng. A three-dimensional discrete element model using arrays of ellipsoids. Géotechnique, 47 (1997), pp. 319-329, 10.1680/geot.1997.47.2.319

[29] J.R. Williams, A.P. Pentland. Supraquadrics and modal dynamics for discrete elements in interactive design. Eng. Comput., 9 (1992), pp. 115-127

[30] I. Rocky DEM, User Manual, 2015.

[31] J. Zhao, T. Shan. Coupled CFD – DEM simulation of fluid – particle interaction in geomechanics. Powder Technol., 239 (2013), pp. 248-258, 10.1016/j.powtec.2013.02.003

[32] M.J. Baker, G.R. Tabor. Computational analysis of transitional air flow through packed columns of spheres using the finite volume technique. Comput. Chem. Eng., 34 (2010), pp. 878-885, 10.1016/j.compchemeng.2009.10.013

[33] L. Hekkala, T. Fabritius, J. Härkki. Mathematical model of heat and mass transfer in the steel belt sintering process. Tenth Int. Ferroalloys Congr. Transform. through Technol., Cape Town (2004), pp. 586-592

[34] M. Nijemeisland, A.G. Dixon. CFD study of fluid flow and wall heat transfer in a fixed bed of spheres. AIChE J., 50 (2004), pp. 906-921, 10.1002/aic.10089

[35] J.D. Anderson. Computational Fluid Dynamics: The Basics with Applications. McGraw-Hill Education, New York (1995)

[36] T.B. Anderson, R. Jackson. Fluid mechanical description of fluidized beds. Equations of motion. Ind. Eng. Chem. Fundam., 6 (1967), pp. 527-539, 10.1021/i160024a007

[37] H. Hertz. Uber die Berhrungfester Elastischer korper. J. Renie Angew Math., 92 (1882), pp. 156-171

[38] R.D. Mindlin. Compliance of elastic bodies in contact. ASME J. Appl. Mech., 16 (1949), pp. 259-268

[39] K.L. Johnson, K. Kendall, A.D. Roberts. Surface energy and the contact of elastic solids. Proc. R. Soc. A Math. Phys. Eng. Sci. (1971), pp. 301-313

[40] C. Thornton, Z. Ning. A theoretical model for the stick/bounce behaviour of adhesive, elastic-plastic spheres. Powder Technol., 99 (1998), pp. 154-162

[41] O.R. Walton. Numerical simulation of inelastic frictional particle–particle interaction. M.C. Roco (Ed.), Part. Two-Phase Flow, Butterworth- Heineman, London, UK (1994), pp. 884-911

[42] J. Sun, F. Battaglia, S. Subramaniam. Dynamics and structures of segregation in a dense, vibrating granular bed. Phys. Rev. E, 74 (2006), pp. 13-14, 10.1103/PhysRevE.74.061307

[43] H. Butt, M. Makowski, M. Kappl, A. Ptak. On the adhesion between individual particles. KONA Powder Part. J., 29 (2011), pp. 53-66

[44] J. Tomas. Adhesion of ultrafine particles—a micromechanical approach. Chem. Eng. Sci., 62 (2007), pp. 1997-2010, 10.1016/j.ces.2006.12.055

[45] I. Itasca. PFC3D User Manual. Minneapolis, USA (2003)

[46] M.J. Jiang, J. Liu, C. Sun, H. Chen. DEM analyses of shear behaviour of rock joints by a novel bond contact model. IOP Conf. Ser. Earth Environ. Sci., 26 (2015), pp. 1-6, 10.1088/1755-1315/26/1/012021

[47] I. Rocky DEM, A brief introduction to DEM and an overview of contact force models in Rocky, 2016.

[48] R. Di Felice. The Voidage function for fluid-particle interaction systems. Int. J. Multiph. Flow., 20 (1994), pp. 153-159

[49] D. Gidaspow, R. Bezburuah, J. Ding. Hydrodynamics of circulating fluidized beds: kinetic theory approach. 7th Eng. Found. Conf. Fluid. Fluid. VII, New York, NY: Engineering Foundation, Brisbane, Australia (1992), pp. 75-82

[50] C.Y. Wen, Y.H. Yu. A generalized method for predicting the minimum fluidization velocity. AIChE J., 12 (1966), pp. 610-612

[51] S. Ergun. Fluid flow through the packed columns. Chem. Eng. Prog., 48 (1952), pp. 89-94

[52] A.M. Nyembwe, R.D. Cromarty, A.M. Garbers-Craig. Effect of concentrate and micropellet additions on iron ore sinter bed permeability. Miner. Process. Extr. Metall., 125 (2016), pp. 178-186, 10.1080/03719553.2016.1180033

[53] W.J. Rankin, P.W. Roller. The measurement of void fraction in beds of granulated iron ore sinter feed. Trans. Iron Steel Inst. Jpn., 25 (1985), pp. 1016-1020, 10.2355/isijinternational1966.25.1016

[54] V. Shatokha, I. Korobeynikov, E. Maire, J. Adrien. Application of 3D X-ray tomography to investigation of structure of sinter mixture granules. Ironmak. Steelmak., 36 (2009), pp. 416-420, 10.1179/174328109X443347

[55] A. Aryaei, K. Hashemnia, K. Jafarpur. Experimental and numerical study of ball size effect on restitution coefficient in low velocity impacts. Int. J. Impact Eng., 37 (2010), pp. 1037-1044

[56] J.L. Meriam, L.G. Kraige. Engineering mechanics dynamics. (fifth ed.), John Wiley & Sons, New York (2002)

[57] M. Marigo, E.H. Stitt. Discrete element method (DEM) for industrial applications: comments on calibration and validation for the modelling of cylindrical pellets. Kona Powder Part. J., 32 (2015), pp. 236-252, 10.14356/kona.2015016

[58] C.J. Coetzee. Review: calibration of the discrete element method. Powder Technol., 310 (2017), pp. 104-142

[59] D. Wang, M. Servin, T. Berglund, K.-O. Mickelsson, S. Rönnbäck. Parametrization and validation of a nonsmooth discrete element method for simulating flows of iron ore green pellets. Powder Technol., 283 (2015), pp. 475-487, 10.1016/j.powtec.2015.05.040

[60] P. Pepiot, O. Desjardins. Numerical analysis of the dynamics of two- and three-dimensional fluidized bed reactors using an Euler-Lagrange approach. Powder Technol., 220 (2012), pp. 104-121, 10.1016/j.powtec.2011.09.021

[61] K.J. Berger, C.M. Hrenya. Challenges of DEM: II. Wide particle size distributions. Powder Technol., 264 (2014), pp. 627-633, 10.1016/j.powtec.2014.04.096

[62] J.K. Su, S.W. Cho, C.C. Yang, R. Huang. Effect of sand ratio on the elastic modulus of self-compacting concrete. J. Mar. Sci. Technol., 10 (2002), pp. 8-13

[63] C.Y. Guan, J.F. Qi, N.S. Qiu, G.C. Zhao, Q. Yang, X.D. Bai, C. Wang. Macroscopic Young's elastic modulus model of particle packing rock layers. Open J. Geol., 2 (2012), pp. 198-202, 10.4236/ojg.2012.23020

[64] I. Keppler, F. Safranyik, I. Oldal. Shear test as calibration experiment for DEM simulations: a sensibility study. Eng. Comput., 33 (2016), pp. 742-758, 10.1108/EC-03-2015-0056